
SimuScene: Simulation-Ready Compositional 3D Scene Reconstruction from a Single Image

Inhee Lee* Sangwon Baik* Sungjoo Kim
Hyeonwoo Kim Hyunsoo Cha Hanbyul Joo†

Seoul National University

*Equal Contribution †Corresponding Author

{ininin0516,bsw1907,masterninja,hwkim408,243stephen,hbjoo}@snu.ac.kr

<https://snucvlab.github.io/SimuScene/>

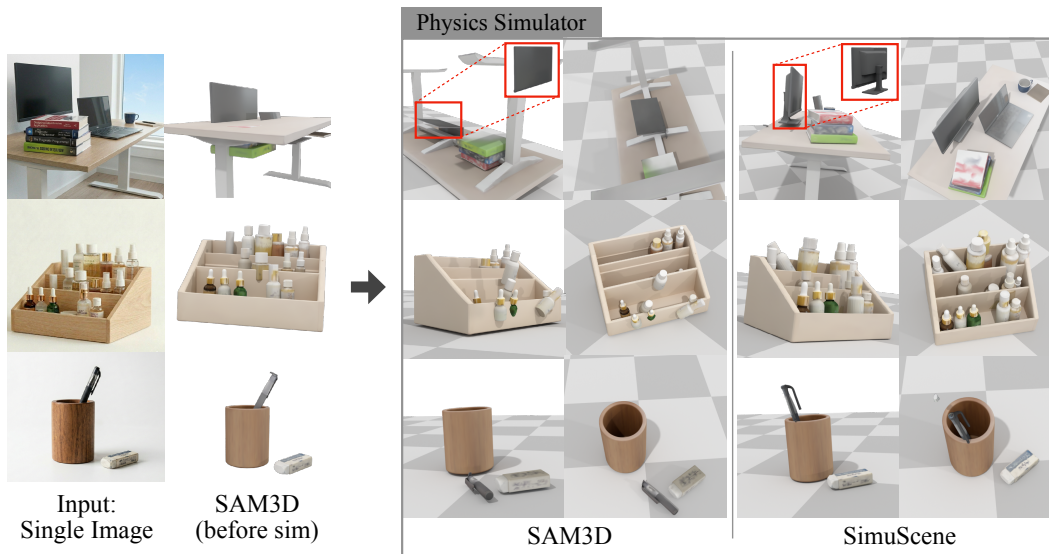


Figure 1: **SimuScene** reconstructs simulation-ready compositional 3D scenes from a single image by using physics simulation to correct object shape and pose. Compared with conventional 3D lifters such as SAM3D [12], our method handles heavy occlusion and produces stable layouts. Red boxes highlight physics-guided shape corrections.

Abstract

Reconstructing interactive, simulation-ready 3D scenes from a single image is a critical bottleneck for robotic manipulation. While recent single-image lifters recover plausible per-object shapes, composing them yields scenes that collapse under physical simulation due to interpenetrating, hovering, or sinking objects. Existing physics-aware methods address this strictly as a post-hoc layout correction, leaving the underlying geometric errors unresolved. To address this, we introduce SimuScene, a compositional 3D reconstruction pipeline that puts physics in the loop of shape and layout estimation. Rather than using physics merely for layout cleanup, we utilize the physics engine as a diagnostic measurement tool during the generative process itself. By diagnostically simulating reconstructed objects under gravity, we convert penetration and support failures into quantitative correction signals that drive gravity-axis stretching and amodal shape resampling. This physics-informed feedback loop mitigates accumulated reconstruction errors and

produces a stable, simulation-ready compositional 3D scene. Extensive experiments demonstrate state-of-the-art performance on physical stability and geometric alignment benchmarks. We further highlight SimuScene’s utility by deploying reconstructed environments in humanoid control and robot-arm manipulation tasks.

1 Introduction

A single photograph of a cluttered desk contains, in principle, everything a robot needs to practice on it: the table to push against, the cup to grasp, the book to slide aside. In practice, however, current methods fall short of extracting this. Single-image scene reconstructors either fuse the entire view into one inseparable mesh [45, 64, 63, 21, 48, 8, 11, 20, 28, 62, 13, 17] or lift each object independently and produce configurations that collapse the moment a physics simulator releases them [27, 39, 12]. Objects sink through tables, hover above shelves, or wedge into one another with overlapping geometry. The difficulty is twofold. A single image is fundamentally ambiguous about occluded geometry and absolute depth, and the physical plausibility that would resolve this ambiguity is not a property any existing dataset readily teaches.

Our goal is to reconstruct a physically plausible, simulation-ready compositional 3D scene from a single image, an output that drops directly into a physics simulator and supports downstream tasks such as reinforcement and imitation learning for robot manipulation, or a VR/AR setup as an interactive 3D scene that responds correctly to contact and gravity. Recent single-image approaches [12] make substantial progress by lifting each detected object into a complete 3D shape. While these results are visually convincing, they are often not physically plausible: once placed in a simulator, objects fall through their supports or explode out of contact, meshes interpenetrate, support relationships break, and objects sink or hover, due to errors in both occlusion-induced shape completion and monocular object pose estimation. Recent efforts [61] begin to incorporate physics into the reconstruction process, yet they apply it only at the layout level, adjusting where each object sits while leaving the underlying shapes untouched. When the geometry itself is incorrect, post-hoc layout adjustment cannot fully recover a plausible configuration. This failure mode also exposes an opportunity: the physics simulation that reveals these artifacts also measures them. For example, the distance an object falls, or the depth at which it interpenetrates a neighbor, gives an important clue to the geometric error that a single view alone cannot supply. Rather than treating these signals as artifacts to clean up at the end, we use them as diagnostic measurements that drive shape correction during reconstruction itself.

We realize this idea in SimuScene, a single-image compositional 3D scene reconstruction pipeline that puts *physics in the loop* of shape and layout estimation. In our pipeline, the physics simulation acts as a diagnostic loop that drives shape and scale correction, not a post-hoc cleanup. The gravity-direction displacement at first contact exposes whether the lifted shape is too short, too tall, or grossly mis-shaped, and feeds directly into the geometry update. We feed this simulator feedback into a resampling stage that recovers more plausible 3D shapes even under heavy occlusion. We further treat the simulator as a source of evidence for shape itself: high stability under simulation correlates with faithful reconstruction, an observation we share with [32] and exploit to reduce the residual uncertainty that occlusion leaves behind. Building on these two roles of physics, SimuScene composes a scene through an iterative, sequential *physics in the loop* procedure that reconstructs one object at a time. Once loaded into a physics simulator, our reconstructions achieve state-of-the-art performance on physical-plausibility and reconstruction-quality metrics. We further demonstrate the resulting object-complete scenes driving downstream applications including humanoid control and robot-arm manipulation tasks.

We make following contributions: (1) **Physics-in-the-loop diagnostic simulation.** A sequential, per-object protocol integrates physical dynamics directly into reconstruction, converting violations (e.g., interpenetration, gravity-induced displacement) into actionable diagnostic signals. (2) **Physics-informed shape correction.** A two-tier geometry update directly addresses these violations via gravity-axis stretching for minor errors and OBB-guided amodal resampling for severe shape failures. (3) **Extensive experimentation.** We provide comprehensive evaluations across diverse datasets and metrics, and show that our reconstructed simulation-ready 3D scenes support downstream robotics applications (i.e. humanoid control policy learning, robot-arm manipulation)

2 Related Work

Multi-Object 3D Reconstruction from Cluttered Images. Recovering a *structured* 3D scene from a single RGB image is ill-posed under occlusion, depth ambiguity, and inter-object interactions, originally tackled by analysis-by-synthesis search over CAD exemplars under structural and physical constraints [25]. End-to-end learning now produces coherent multi-object geometry from a single view via feed-forward regression with non-intersecting outputs [43], multi-instance diffusion with cross-instance attention [27], hierarchical isometric-view amodal completion [14], or promptable scene-level reconstruction [12], while divide-and-conquer pipelines reconstruct each object independently and reassemble them via iterative occlusion removal [2], differentiable optimal-transport alignment [19], or feed-forward decoupling of appearance, rotation, scale, and translation [24]. Despite improving geometric fidelity and instance separation, the resulting assets routinely interpenetrate, float, or fail to satisfy support relations, leaving the scenes unsuitable for downstream simulation and embodied use.

Physics-Aware Scene Reconstruction and Simulation-in-the-Loop Refinement. Physics constraints have long shaped reconstruction, from early scene parsers that encode support and collision feasibility in the inference objective [25] to recent physics-aware and differentiable-simulation pipelines that jointly optimize geometry, pose, material, or appearance via physically plausible implicit surfaces [40], MPM-driven compositional Gaussian generation [58], amodal MPM-coupled scene reconstruction [10], or human-scene depth-alignment and contact priors [57], with simulator feedback also serving as a reward-style alignment signal for image-to-3D generators [32]. At the scene level, relation-graph rigid-body solvers [61] and simulator-in-the-loop assembly [56] resolve penetration and floating artifacts in assembled layouts, while text-conditioned generators embed SDF collision avoidance, gravity, or differentiable rigid-body simulation directly in the generation loop to produce intersection-free, statically stable scenes [35, 31, 34].

Direct Preference Optimization for Generative Models. Direct Preference Optimization (DPO) replaces the reward modeling and on-policy RL step of RLHF [41] with a simple preference-classification objective derived from a closed-form reparameterization of the Bradley–Terry reward model [44]. Subsequent language-model alignment methods generalize this objective [4], replace pairwise preferences with binary utility feedback [15], integrate preference optimization into supervised fine-tuning [22], or remove the reference model through a length-normalized reward with a target margin [38]. For visual generation, Diffusion-DPO [52] adapts DPO to diffusion models by replacing autoregressive log-likelihood ratios with denoising-loss differences, while related methods formulate denoising as a policy optimization problem [60, 7] or introduce step-wise preference comparisons [33]. At the 3D level, DSO [32] uses rigid-body simulation feedback to fine-tune image-to-3D generators for physical soundness with DPO or DRO objectives. Inspired by DSO and Diffusion-DPO, we fine-tune the SAM3D shape branch with a flow-matching DPO objective over synthetic occlusion-versus-amodal-completion pairs. Unlike DSO, which optimizes standalone object stability, our preference signal targets occlusion-robust shape resampling for objects in cluttered scenes.

3 Method

Given a single RGB image I , our goal is to reconstruct a simulation-ready compositional 3D scene \mathcal{S} , visually aligned with I and physically consistent under gravity:

$$\mathcal{S} = \{\mathcal{M}_i, s_i, \mathbf{t}_i, \mathbf{R}_i\}_{i=1}^N, \tag{1}$$

where \mathcal{M}_i is a 3D canonical mesh for i -th object, $s_i \in \mathbb{R}^+$ is an isotropic scale of \mathcal{M}_i , $\mathbf{t}_i \in \mathbb{R}^3$ and $\mathbf{R}_i \in \text{SO}(3)$ are a translation vector and a rotation matrix of \mathcal{M}_i , and N is the number of objects in the scene. Monocular ambiguity and occlusion often cause penetration, floating, and toppling; we therefore use diagnostic physics signals to refine object poses and correct geometry through Oriented Bounding Box (OBB)-guided stretching or resampling. Fig. 2 summarizes our pipeline.

3.1 Decomposed Scene Initialization

Because base structures (e.g., tables, shelves) support most objects in cluttered scenes, we reconstruct them separately from other objects. We first remove non-base objects with an MLLM-based image

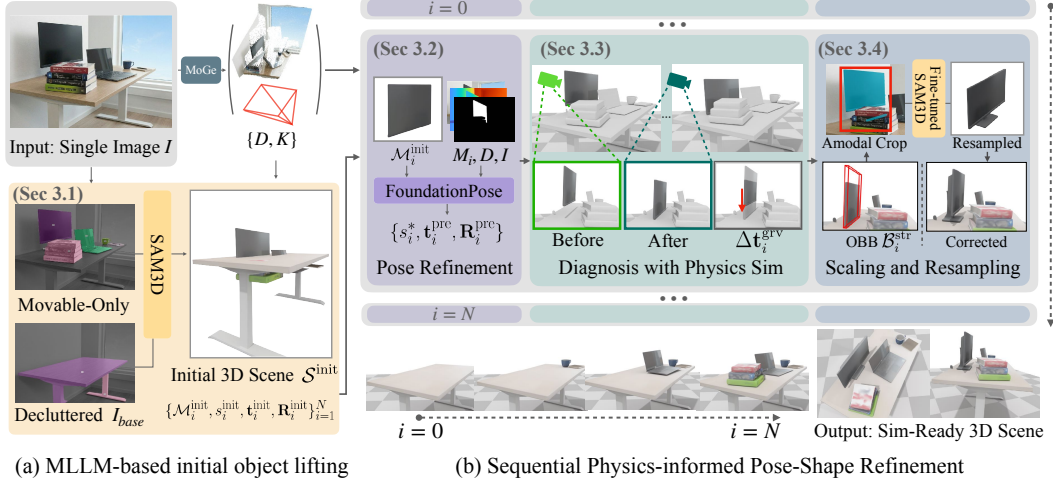


Figure 2: **Pipeline Overview.** (a) From a single image I , foundation priors decompose the scene into object meshes with poses. (b) Each object then passes through pose initialization, diagnostic physics simulation, and shape correction; completed objects are frozen as colliders, and physics displacements drive the correction. The corrected objects settle into a simulation-ready 3D scene.

editor [50] and run SAM3D [12] on the decluttered image I_{base} to obtain fixed base colliders. For the remaining objects, RAM++ [26] and a VLM [1] generate instance labels, SAM3 [9] produces masks M_i , and SAM3D, denoted by Φ , lifts each instance:

$$\Phi(I, M_i, I_{M_i}, D) = (\mathcal{M}_i^{\text{init}}, s_i^{\text{init}}, \mathbf{t}_i^{\text{init}}, \mathbf{R}_i^{\text{init}}), \quad (2)$$

where M_i is the segmentation mask of i -th object, I_{M_i} is the masked image crop, and D is single-view depth from MoGe [53]. $\mathcal{M}_i^{\text{init}}$ is in SAM3D’s canonical frame, with its AABB centered at the origin and the longest side normalized to 1. Beyond geometry, we extract semantic information that proves critical for physics. The VLM tags each object with one of three pose-DoF labels, *free* (6-DoF), *point-anchored* (3-DoF rotation about a wall point), or *line-anchored* (1-DoF rotation about the anchor line). These tags tell the simulator which constraints to apply to each object. Since the floor and walls are fixed after initial estimation, we omit them from Eq. (1) for simplicity. See Sec. A.1 for additional details on scene decomposition.

3.2 Pose Refinement Before Simulation

SAM3D produces plausible shapes but in its own canonical frame, with poses only approximately consistent with the image. Handing these poses directly to a physics simulator amplifies even small rotational errors into severe penetration and contact artifacts. We therefore refine each object’s pose against image evidence before simulation. We obtain depth D and camera intrinsics K from I using MoGe [53], and back-project the pixels inside the segmentation mask M_i to form the object point cloud $\mathcal{P}_i \in \mathbb{R}^{P \times 3}$. We first solve for (s_i^*, \mathbf{t}_i^*) by aligning the canonical mesh $\mathcal{M}_i^{\text{init}}$ with \mathcal{P}_i (see Sec. A.1 for details). Rotation, however, cannot be reliably recovered from point-cloud alignment alone, so we hand the result to FoundationPose [54] for refinement:

$$(\mathbf{t}_i^{\text{pre}}, \mathbf{R}_i^{\text{pre}}) = \text{FoundationPose}(I, D, K, M_i, s_i^* \mathcal{M}_i^{\text{init}}, \mathbf{t}_i^*, \mathbf{R}_i^{\text{init}}), \quad (3)$$

where $s_i^* \mathcal{M}_i^{\text{init}}$ denotes $\mathcal{M}_i^{\text{init}}$ scaled by s_i^* , and \mathbf{t}_i^* and $\mathbf{R}_i^{\text{init}}$ from the previous alignment are used for the initials. The pre-simulation scene is then composed as:

$$\mathcal{S}^{\text{pre}} = \{\mathcal{M}_i^{\text{init}}, s_i^*, \mathbf{t}_i^{\text{pre}}, \mathbf{R}_i^{\text{pre}}\}_{i=1}^N. \quad (4)$$

3.3 Diagnostic Simulation: Physics as a Probe

The pre-simulation scene \mathcal{S}^{pre} is the image-faithful configuration we can produce from perception alone, but it is not yet physically valid. It still contains penetrations and floating objects rooted in

monocular reconstruction ambiguity, and as shown in Fig. 4, naively dropping everything under gravity produces chaotic dynamics in which mutually penetrating objects push each other into impossible configurations. We use physics simulation to diagnose these residual errors: we first resolve inter-object penetration by displacing the target object along a simulator-informed direction. Then, after releasing the object under gravity, the resulting displacement and contact signals expose unresolved gravity-axis shape and support errors that drive the shape-correction stage (Sec. 3.4).

To keep the diagnostic signal clean and avoid joint-settling deadlocks, we compose the scene with a sequential protocol. Objects are processed in ascending order of the lowest corner of their world-frame bounding box along the gravity direction. For each active object i , only that object is dynamic, while previously placed objects are frozen as static colliders, and the simulation halts at the first frame of contact. This prevents mutually penetrating objects from pushing each other into impossible configurations and avoids unstable trajectories that drift far from the image-aligned pose.

Penetration Resolution. For simplicity, we assume that objects are indexed according to the sequential processing order, so that object i is processed after objects $1, \dots, i-1$. For each active object i , the simulator generates a penetration-resolving displacement $\Delta \mathbf{t}_i^{\text{pen}}$ to prevent overlap with the previously processed objects $1, \dots, i-1$. For the first object, the procedure resolves penetration with the floor and any walls. The scene after penetration resolution, denoted by \mathcal{S}^{pen} , is formulated as

$$\mathcal{S}^{\text{pen}} = \{\mathcal{M}_i^{\text{init}}, s_i^*, \mathbf{t}_i^{\text{pre}} + \Delta \mathbf{t}_i^{\text{pen}}, \mathbf{R}_i^{\text{pre}}\}_{i=1}^N. \quad (5)$$

Objects whose pose-DoF tag is *point-anchored* or *line-anchored* are anchored at their current positions using the procedure described in Sec. A.3. Accordingly, as discussed in Sec. 3.1, objects tagged as *point-anchored* are restricted to 3-DoF rotation about the anchor point, while objects tagged as *line-anchored* are restricted to 1-DoF rotation about the anchor line.

Gravity-Based Diagnostics. We then sequentially release each active object i under gravity. If the pose-DoF tag of the object is *free*, the object is frozen at the first simulation frame in which it contacts any surface, yielding the gravity-induced displacement $\Delta \mathbf{t}_i^{\text{grv}}$. For wall-anchored objects, i.e., those tagged as *point-anchored* or *line-anchored*, the object is simulated under its corresponding rotational constraint until it settles under gravity, yielding the gravity-induced rotation $\Delta \mathbf{R}_i^{\text{grv}}$. The resulting post-simulation scene \mathcal{S}^{sim} is formulated as

$$\mathcal{S}^{\text{sim}} = \{\mathcal{M}_i^{\text{init}}, s_i^*, \mathbf{t}_i^{\text{pre}} + \Delta \mathbf{t}_i^{\text{pen}} + \Delta \mathbf{t}_i^{\text{grv}}, \Delta \mathbf{R}_i^{\text{grv}} \mathbf{R}_i^{\text{pre}}\}_{i=1}^N. \quad (6)$$

Here, $\Delta \mathbf{R}_i^{\text{grv}}$ is the identity matrix for objects tagged as *free*. For wall-anchored objects, the constrained simulation returns the full pose change $(\Delta \mathbf{t}_i^{\text{grv}}, \Delta \mathbf{R}_i^{\text{grv}})$ induced by rotation about the anchor.

Displacement-Based Shape Correction Criterion. We use the physics-induced translation as a diagnostic signal for shape correction. First, we compute the object’s OBB (Oriented Bounding Box) in the pre-simulation scene \mathcal{S}^{pre} :

$$\mathcal{B}_i^{\text{pre}} = \text{OBB}(\mathbf{R}_i^{\text{pre}} (s_i^* \mathcal{M}_i^{\text{init}}) + \mathbf{t}_i^{\text{pre}}). \quad (7)$$

Let ℓ_i^{pre} be the side length of $\mathcal{B}_i^{\text{pre}}$ along the OBB axis most aligned with the unit gravity direction $\hat{\mathbf{g}}$. We then define the normalized gravity-axis displacement as

$$\rho_i = \frac{|\hat{\mathbf{g}}^\top (\Delta \mathbf{t}_i^{\text{pen}} + \Delta \mathbf{t}_i^{\text{grv}})|}{\ell_i^{\text{pre}}}. \quad (8)$$

ρ_i measures how much each object in the post-simulation scene \mathcal{S}^{sim} deviates from its counterpart in the pre-simulation scene \mathcal{S}^{pre} , which is the scene most closely aligned with the input image. When ρ_i is small, we regard the deviation as the result of minor errors accumulated through the pipeline and correct the scene with a lightweight adjustment. In contrast, when ρ_i is large, we attribute the deviation to a more fundamental shape-sampling failure, since our pipeline already performs substantial pose refinement. Specifically, if $\rho_i \geq 0.15$, we attribute the error to an unreliable SAM3D shape sample and trigger shape resampling; otherwise, we correct the object by stretching it along the gravity-aligned OBB axis.

3.4 Physics-Informed Shape Correction

Gravity-axis Stretch. When $\rho_i < 0.15$, we regard the discrepancy between \mathcal{S}^{pre} and \mathcal{S}^{sim} as a small accumulated error and correct it with a lightweight stretch rather than resampling. Let $\hat{\mathbf{u}}_i^{\text{grv}}$ be

the OBB axis of $\mathcal{B}_i^{\text{pre}}$ most aligned with the gravity direction $\hat{\mathbf{g}}$, and let $\hat{\mathbf{a}}_i^{\text{grv}} = (\mathbf{R}_i^{\text{pre}})^\top \hat{\mathbf{u}}_i^{\text{grv}}$ be the corresponding axis in the canonical mesh frame. We use the signed gravity-axis displacement

$$\eta_i = \frac{\hat{\mathbf{g}}^\top (\Delta \mathbf{t}_i^{\text{pen}} + \Delta \mathbf{t}_i^{\text{grv}})}{\ell_i^{\text{pre}}} \quad (9)$$

to stretch the canonical mesh along $\hat{\mathbf{a}}_i^{\text{grv}}$. The stretched mesh is then renormalized to preserve the canonical-mesh convention, with the normalization absorbed into the object scale; the translation is updated so that the OBB face opposite to gravity remains fixed. This yields the stretched object $(\mathcal{M}_i^{\text{str}}, s_i^{\text{str}}, \mathbf{t}_i^{\text{str}}, \Delta \mathbf{R}_i^{\text{grv}} \mathbf{R}_i^{\text{pre}})$. See Sec. A.4 for details.

Amodal Shape Resampling. When $\rho_i \geq 0.15$, we attribute the error to an unreliable SAM3D shape sample, which typically occurs when severe occlusion causes SAM3D to fail at amodal shape completion. We compute a desired OBB $\mathcal{B}_i^{\text{str}}$ by stretching $\mathcal{B}_i^{\text{pre}}$ along the gravity axis by the simulated displacement, and use it to guide shape resampling. Since the true amodal mask is unavailable, we construct an auxiliary crop mask M'_i by augmenting the modal segmentation mask M_i with the projected lowest part of $\mathcal{B}_i^{\text{str}}$, as shown in Fig. 2. Although M'_i is not a true amodal segmentation mask, it yields an amodal crop image $I_{M'_i}$ that covers the expected hidden extent of the target object. We then run SAM3D with this physics-informed crop:

$$\Phi(I, M_i, I_{M'_i}, D) = (\mathcal{M}_i^{\text{re}}, s_i^{\text{re}}, \tilde{\mathbf{t}}_i^{\text{re}}, \mathbf{R}_i^{\text{re}}). \quad (10)$$

Since the resampled shape has different canonical geometry and scale, the previous scale and rotation are no longer valid, while the desired OBB $\mathcal{B}_i^{\text{str}}$ provides the target object location. We therefore keep the resampled mesh, scale, and rotation from SAM3D, but set the translation to the OBB center, $\mathbf{t}_i^{\text{re}} := \text{center}(\mathcal{B}_i^{\text{str}})$. The resulting resampled object is represented as $(\mathcal{M}_i^{\text{re}}, s_i^{\text{re}}, \mathbf{t}_i^{\text{re}}, \mathbf{R}_i^{\text{re}})$.

SAM3D Fine-tuning for Amodal Resampling. To make SAM3D robust to the resampling input in Eq. (10), we fine-tune it with synthetic preference pairs that contrast occlusion-failed shape latents against edited full-object completion latents.

We fine-tune SAM3D using a DPO-style objective [32, 44, 52] that compares the flow-matching [36] losses of preferred and rejected shape latents:

$$\mathcal{L}_{\text{FM-DPO}}(\theta) = \mathbb{E}_i \left[w_i \left(-\log \sigma \left(-\frac{\beta}{2} (d_{\theta,i} - d_{\text{ref},i}) \right) \right) \right], \quad (11)$$

where w_i is the sample weight, σ is the sigmoid function, β controls the preference strength, $d_{\theta,i}$ is the win-lose flow-matching loss difference of the current model, and $d_{\text{ref},i}$ is the corresponding difference computed by the frozen base SAM3D reference model. This objective encourages the fine-tuned model to assign a lower relative flow-matching loss to the completed amodal latent than to the occlusion-failed latent. To preserve the base model, we do not update the full SAM3D generator; instead, we train only LoRA [23] adapters inserted into the attention projections of the shape generation branch. Details of preference-pair construction, loss definitions, and training weights are provided in the Sec. A.4.

3.5 Final Composition

The preceding stages produce corrected object states, but they do not yet define the final simulation-ready layout: the diagnostic simulation in Sec. 3.3 is designed to extract clean correction signals, whereas the final scene must be physically settled under the object’s full pose constraints. We first assemble each object from its corrected state. Wall-anchored objects retain the initial geometry and use the constrained pose obtained from diagnostic simulation: $(\mathcal{M}_i^{\text{init}}, s_i^*, \mathbf{t}_i^{\text{pre}} + \Delta \mathbf{t}_i^{\text{pen}} + \Delta \mathbf{t}_i^{\text{grv}}, \Delta \mathbf{R}_i^{\text{grv}} \mathbf{R}_i^{\text{pre}})$. Free objects are replaced by either the stretched state $(\mathcal{M}_i^{\text{str}}, s_i^{\text{str}}, \mathbf{t}_i^{\text{str}}, \Delta \mathbf{R}_i^{\text{grv}} \mathbf{R}_i^{\text{pre}})$ or the resampled state $(\mathcal{M}_i^{\text{re}}, s_i^{\text{re}}, \mathbf{t}_i^{\text{re}}, \mathbf{R}_i^{\text{re}})$, according to the correction branch selected in Sec. 3.3. Starting from these assembled states, we rerun sequential penetration resolution to remove residual overlaps introduced by shape correction. Unlike the diagnostic probe, the final simulation does not freeze free objects at first contact. Instead, free objects are simulated as full 6-DoF rigid bodies, while *point-anchored* and *line-anchored* objects follow their corresponding rotational constraints. After all objects settle under gravity, the resulting stable configuration defines the final simulation-ready compositional 3D scene \mathcal{S} .

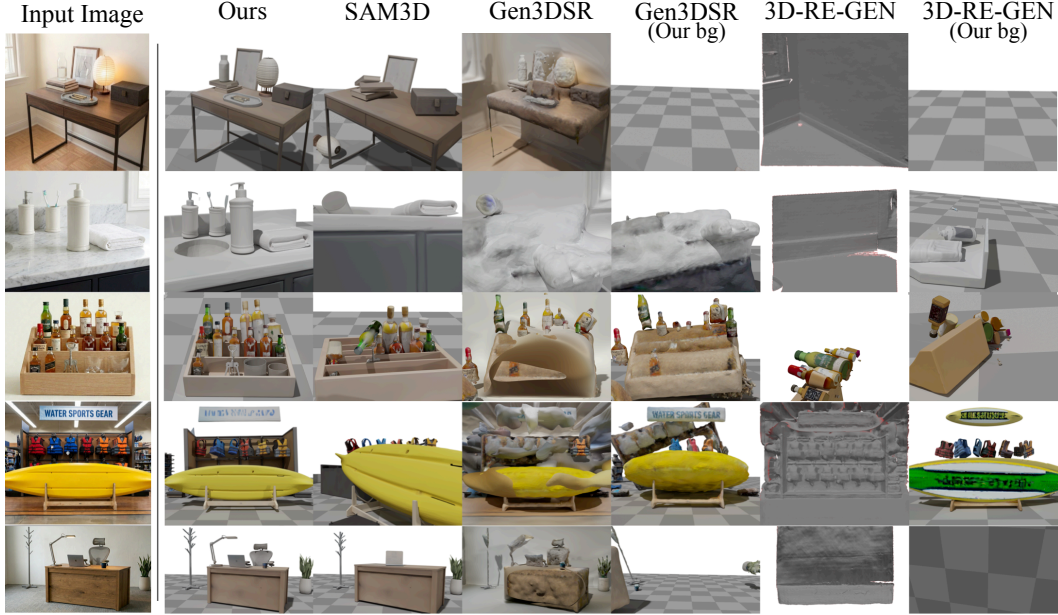


Figure 3: **Qualitative Comparison of GenWild.** All scenes are visualized after gravity-driven physics simulation. Baselines either remain artificially stuck mid-air due to interpenetration or collapse catastrophically, while our method preserves both physical plausibility and input-view alignment in cluttered scenes.

Method	GraspClutter6D [5]					AriaDigitalTwin [42]					GenWild				
	ABO _{th/fo} ↑	ABO ↑	D_{mean} ↓	E_{pk} ↓	Penetr. ↓	3D ABO _{th/fo} ↑	3D ABO ↑	D_{mean} ↓	E_{pk} ↓	Penetr. ↓	ABO _{th/fo} ↑	ABO ↑	D_{mean} ↓	E_{pk} ↓	Penetr. ↓
SAM3D [12]	0.087	0.121	0.638	4.064	24.5%	0.051	0.069	0.721	3.556	16.4%	0.218	0.263	0.555	2.957	16.2%
Gen3DSR [3]	0.014	0.219	0.267	1.587	75.8%	0.012	0.242	0.091	0.556	93.3%	0.046	0.480	0.255	1.214	72.7%
Gen3DSR [3] (our bg)	0.014	0.036	0.880	5.644	50.3%	0.190	0.242	0.932	5.769	17.2%	0.105	0.145	0.817	5.230	16.9%
3D-RE-GEN [46]	0.023	0.035	0.945	5.757	26.0%	0.069	0.091	0.879	5.093	17.2%	0.009	0.012	0.957	3.639	14.7%
3D-RE-GEN [46] (our bg)	0.048	0.078	0.765	4.265	30.1%	0.067	0.091	0.830	4.130	17.4%	0.124	0.158	0.554	3.120	18.3%
Ours	0.248	0.267	0.250	1.092	10.3%	0.293	0.338	0.310	1.370	8.8%	0.507	0.532	0.128	0.420	2.5%

Table 1: **Main quantitative comparison.** 2D alignment and physical stability on GraspClutter6D [5] and GenWild, and 3D alignment on AriaDigitalTwin [42]. Penetr. reports the penetrated object ratio; columns marked ↑ (↓) indicate higher (lower) is better.

4 Experiments

4.1 Experimental Setup

Implementation Details. For physical simulation and evaluation, we employ MuJoCo [51] and extract collision geometries for each reconstructed object using V-HACD. For SAM3D fine-tuning, we use 16.6K cached latent preference pairs, with 8.3K occlusion-completion pairs and 8.3K clean preservation pairs. The pair weights w_i in Eq. (11) are set to 1.0 and 0.1, respectively, and we use $\beta = 500$. We freeze the pretrained SAM3D model as θ_{ref} and fine-tune only shape-branch LoRA [23] adapters in the Stage-1 MM-DiT backbone, applying the flow-matching loss only to the Stage-1 shape latent. The adapters use rank $r = 64$, scaling $\alpha = 128$, no dropout, and are applied to 120 linear layers across 24 transformer blocks. We train with AdamW [37] using a global batch size of 16 on four NVIDIA RTX PRO 6000 Blackwell GPUs, a learning rate of 1×10^{-5} after 300 warmup steps, weight decay 0.01, gradient clipping at 1.0, and bfloat16 mixed precision for 1,500 steps.

Datasets. To comprehensively evaluate complex multi-object composition and physical stability, we assemble three complementary test sources:

- **GraspClutter6D [5]:** We use the released YCB-V test scene split of GraspClutter6D, which contains 94 real cluttered scenes. For each scene, we select a single RGB view by computing the union bounding box of all provided visible object masks and choosing the view with the largest total margin to the image boundary, thereby avoiding views with frame-truncated objects. We use

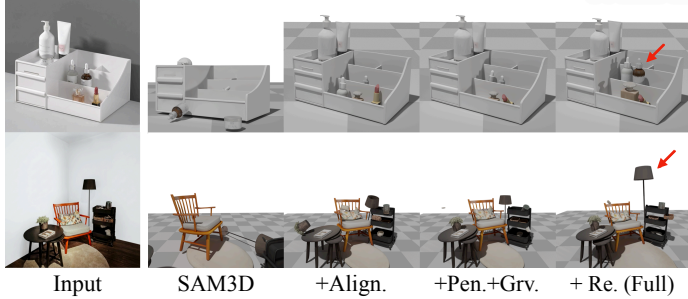


Figure 4: **Qualitative Ablation.** Post-simulation rendering of 3D scene. From SAM3D, we progressively add per-object alignment (Align.), penetration resolution (Pen.), stabilized gravity simulation (Grv.), and shape resampling (Re.). The red arrows indicate that resampling successfully generates plausible, aligned shapes.

Variants	ABO \uparrow	ABO _{fh/fo} \uparrow	D_{mean} \downarrow
SAM3D	0.263	0.218	0.555
+Align.	0.409	0.361	0.364
+Pen.	0.403	0.372	0.395
+Grv.	0.440	0.406	0.197
+Re. (Full)	0.532	0.507	0.128

Table 2: **Quantitative Ablation.** The column order matches Fig. 4. Each stage improves the overall post-simulation alignment and stability, with our full model (+Re.) performing best.

Metric	Ours	SAM3D	Stretched
Elo \uparrow	1083.4	931.5	908.9
Win Rate (%) \uparrow	71.9	41.3	36.8

Table 3: **Mesh Completion Quality.** VLM-based mesh quality evaluation [55] on GenWild. Win Rate is the average pairwise win rate against the other candidates.

- the provided visible instance masks as ground-truth masks for foreground objects, and additionally obtain masks for unannotated supporting structures (i.e. tables, boxes, and shelves) using SAM3.
- **Aria Digital Twin (ADT)** [42]: We sample 40 static scenes, explicitly filtering out sequences with humans or moving objects (details in Sec. B.3). This dataset not only provides per-instance 3D ground-truth meshes and 6-DoF poses for rigorous quantitative evaluation, but also allows us to assess the physical stability of complex spatial arrangements at the full scene level.
 - **GenWild:** To introduce diverse, out-of-distribution physical arrangements, we generate 50 synthetic images via text and image prompts [50], depicting highly challenging everyday layouts.

Evaluation Metrics. Our evaluation rests on a core philosophy: evaluating initial visual alignment or physical stability in isolation is misleading. Visual fidelity is meaningless if scenes immediately collapse under physics, while trivial stability (e.g., naively projecting objects onto the floor) destroys original spatial intents. We resolve this trade-off by measuring spatial alignment *post-simulation* [51]. Measuring alignment only after dynamics settle naturally penalizes both physical collapses and distorted layouts, ensuring input-faithful simulation-ready reconstructions. We evaluate physical stability using Mean Displacement (D_{mean}) for residual settling errors, Peak Energy (E_{pk}) for dynamic artifacts, and penetration ratio (Penetr.). For view alignment, we compute Average Best Overlap (ABO). Since standard ABO artificially rewards physically interpenetrating objects, we introduce strict variants— ABO_{fo} (free objects) and ABO_{fh} (free and hanging)—which explicitly zero out scores for invalid instances. See Sec. B.1 for detailed metric formulations.

Baselines. We compare against methods capable of input-view aligned compositional reconstruction: SAM3D [12], Gen3DSR [3], and 3D-RE-GEN [46], all evaluated using identical MuJoCo parameters and the same kinematic DoF tags to prevent unfair simulation penalties for hanging objects. Because flawed baseline backgrounds (e.g., missing floors) often trigger immediate simulation collapse, we evaluate the compositional baselines twice: with their native backgrounds, and with our wall/floor base mesh substituted in (*our bg*) to fairly isolate core object reconstruction quality.

4.2 Experimental Results

Quantitative Comparison. As shown in Tab. 1, our method achieves state-of-the-art results across all datasets, yielding the highest $ABO_{\text{fh/fo}}$ and lowest penetration ratios. While Gen3DSR [3] records a deceptively high standard ABO, its severe penetration reveals physically fused objects, causing its scores to drop significantly under our strict $ABO_{\text{fh/fo}}$ metrics. Furthermore, since baselines often lack physically accurate environments, we evaluate them by supplying our extracted boundary constraints (*our bg*). Interacting with these proper solid boundaries fully exposes their inherent instability. For

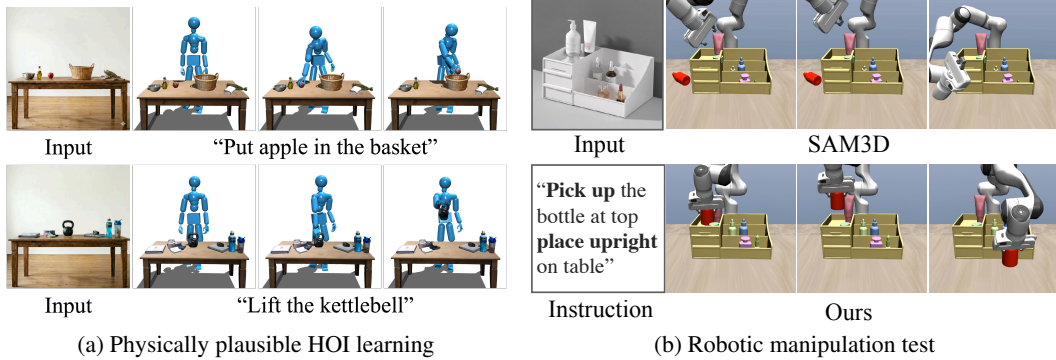


Figure 5: **Applications.** Two downstream uses of our object-complete physics-stable reconstructions: (a) physics-based character control [29], (b) cluttered robotic manipulation [6].

3D-RE-GEN, we replace its background mesh with our wall boundary while retaining its native floor parameters; despite this setup, its objects still fail to settle stably and maintain high energy errors.

Qualitative Results. Visual comparisons in Fig. 3 confirm these quantitative trends. As baselines frequently fuse objects together or embed them into the background, their high penetration ratios cause severe collisions during simulation, scattering objects out of bounds and resulting in completely missing meshes in their visualizations. In contrast, our pipeline places reconstructed objects in precise, static alignment with the input image, faithfully preserving the original spatial layout. Even heavily occluded items are accurately anchored to their exact locations with complete 3D geometry.

4.3 Ablation Study

The ablation results on the GenWild presented in Tab. 2 and Fig. 4, demonstrate our pipeline’s effectiveness by progressively adding components. Adding object pose alignment (**+Align.**) yields the largest initial improvement by improving visual alignment and resolving deep interpenetrations. Subsequently applying rigid physics (**+Pen.+Grv.**) stabilizes dynamics, but fundamentally incorrect geometries still persist. Finally, incorporating physics-informed shape correction (**+Re.**) successfully resolves these remaining distortions; as observed, replacing flawed meshes via amodal resampling directly translates to the lowest displacement error and highest alignment scores. Beyond layout stability, we validate whether our fine-tuned amodal resampler realistically completes occluded geometries. For all objects triggering resampling, a VLM-based pairwise comparison [55] evaluates which rendered mesh provides a more plausible shape completion given the input context. As shown in Tab. 3, our amodal resampling achieves a substantially higher Elo score and win rate over the raw SAM3D baseline and simple stretching operations, confirming its superior ability to recover complete, visually plausible 3D shapes.

4.4 Applications

Our physically stable 3D reconstruction unlocks a single capability: the scene can be dropped into any simulator as a collection of separately addressable rigid bodies with consistent contact geometry, with no manual scene-authoring step. Fig. 5 presents two downstream systems built on this invariant.

Physics-Based Character Control. We load reconstructed scenes into a physics simulator and train a humanoid control policy following DeVi [29]. As our scene provides physically stable assets, we are able to generate physics-based character motion including dexterous human-object interaction (HOI) in a novel scene by leveraging a video diffusion model as an HOI-aware motion planner.

Robot-arm Manipulation We use our reconstructions as input to a closed-loop VLM agent [6] for text-guided 6D pose prediction, with execution carried out by GraspNet-based grasping [16] and OMPL motion planning [49]. Whereas naive SAM3D leaves occluded geometry incomplete, with objects breaking away from their image-observed positions, our image-aligned reconstructions are object-complete and physically grounded, providing stable grasp targets and collision-free trajectories. The reconstructed scenes therefore serve as a controllable test bed for text-guided robot-arm manipulation.

5 Discussion

We reframe physical simulation from a post-hoc validator into an in-the-loop diagnostic signal that inverts physical violations into geometric corrections, resolving the structural ambiguities of monocular perception. The resulting scenes are directly usable in downstream tasks such as robotic manipulation and reinforcement learning. While our sequential protocol cannot revise early estimates from later evidence, integrating physical dynamics as a generative supervisory signal offers a scalable foundation for reconstructing simulation-ready scenes from single images, with joint scene-level optimization as a natural next step.

References

- [1] Josh Achiam, Steven Adler, Sandhini Agarwal, Lama Ahmad, Ilge Akkaya, Florencia Leoni Aleman, Diogo Almeida, Janko Altenschmidt, Sam Altman, Shyamal Anadkat, et al. Gpt-4 technical report. *arXiv preprint arXiv:2303.08774*, 2023. [4](#), [19](#)
- [2] Rio Aguina-Kang, Kevin James Blackburn-Matzen, Thibault Groueix, Vladimir Kim, and Matheus Gadelha. Seeing through clutter: Structured 3d scene reconstruction via iterative object removal. In *3DV*, 2026. [3](#)
- [3] Andreea Ardelean, Mert Özer, and Bernhard Egger. Gen3dsr: Generalizable 3d scene reconstruction via divide and conquer from a single view. In *3DV*, 2025. [7](#), [8](#), [14](#), [21](#)
- [4] Mohammad Gheshlaghi Azar, Zhaohan Daniel Guo, Bilal Piot, Remi Munos, Mark Rowland, Michal Valko, and Daniele Calandriello. A general theoretical paradigm to understand learning from human preferences. In *AISTATS*, 2024. [3](#)
- [5] Seunghyeok Back, Joosoon Lee, Kangmin Kim, Heeseon Rho, Geonhyup Lee, Raeyoung Kang, Sangbeom Lee, Sangjun Noh, Youngjin Lee, Taeyeop Lee, et al. Graspclutter6d: A large-scale real-world dataset for robust perception and grasping in cluttered scenes. *RA-L*, 2025. [7](#), [14](#), [21](#), [22](#)
- [6] Sangwon Baik, Gunhee Kim, Mingi Choi, and Hanbyul Joo. Text-guided 6d object pose rearrangement via closed-loop vlm agents. *arXiv:2604.09781*, 2026. [9](#), [21](#)
- [7] Kevin Black, Michael Janner, Yilun Du, Ilya Kostrikov, and Sergey Levine. Training diffusion models with reinforcement learning. *arXiv preprint arXiv:2305.13301*, 2023. [3](#)
- [8] Andreas Blattmann, Tim Dockhorn, Sumith Kulal, Daniel Mendelevitch, Maciej Kilian, Dominik Lorenz, Yam Levi, Zion English, Vikram Voleti, Adam Letts, et al. Stable video diffusion: Scaling latent video diffusion models to large datasets. *arXiv preprint arXiv:2311.15127*, 2023. [2](#)
- [9] Nicolas Carion, Laura Gustafson, Yuan-Ting Hu, Shoubhik Debnath, Ronghang Hu, Didac Suris, Chaitanya Ryali, Kalyan Vasudev Alwala, Haitham Khedr, Andrew Huang, et al. Sam 3: Segment anything with concepts. *arXiv preprint arXiv:2511.16719*, 2025. [4](#)
- [10] Boyuan Chen, Hanxiao Jiang, Shaowei Liu, Saurabh Gupta, Yunzhu Li, Hao Zhao, and Shenlong Wang. Physgen3d: Crafting a miniature interactive world from a single image. In *CVPR*, 2025. [3](#)
- [11] Haoxin Chen, Yong Zhang, Xiaodong Cun, Menghan Xia, Xintao Wang, Chao Weng, and Ying Shan. Videocrafter2: Overcoming data limitations for high-quality video diffusion models. In *CVPR*, 2024. [2](#)
- [12] Xingyu Chen, Fu-Jen Chu, Pierre Gleize, Kevin J Liang, Alexander Sax, Hao Tang, Weiyao Wang, Michelle Guo, Thibaut Hardin, Xiang Li, et al. Sam 3d: 3dfy anything in images. *arXiv preprint arXiv:2511.16624*, 2025. [1](#), [2](#), [3](#), [4](#), [7](#), [8](#), [14](#), [21](#)
- [13] Jaeyoung Chung, Suyoung Lee, Hyeongjin Nam, Jaerin Lee, and Kyoung Mu Lee. Luciddreamer: Domain-free generation of 3d gaussian splatting scenes. *TVCG*, 2025. [2](#)
- [14] Wenqi Dong, Bangbang Yang, Zesong Yang, Yuan Li, Tao Hu, Hujun Bao, Yuewen Ma, and Zhaopeng Cui. Hiscene: creating hierarchical 3d scenes with isometric view generation. In *ACMMM*, 2025. [3](#)
- [15] Kawin Ethayarajh, Winnie Xu, Niklas Muennighoff, Dan Jurafsky, and Douwe Kiela. Kto: Model alignment as prospect theoretic optimization. *arXiv preprint arXiv:2402.01306*, 2024. [3](#)
- [16] Hao-Shu Fang, Chenxi Wang, Minghao Gou, and Cewu Lu. Graspnet-1billion: A large-scale benchmark for general object grasping. In *ICCV*, 2020. [9](#), [21](#)

- [17] Ruiqi Gao, Aleksander Holynski, Philipp Henzler, Arthur Brussee, Ricardo Martin-Brualla, Pratul Sriniwasan, Jonathan T Barron, and Ben Poole. Cat3d: Create anything in 3d with multi-view diffusion models. *arXiv preprint arXiv:2405.10314*, 2024. 2
- [18] Google AI Edge. Mediapipe solutions guide. <https://developers.google.com/mediapipe>, 2025. 21
- [19] Haonan Han, Rui Yang, Huan Liao, Jiankai Xing, Zunnan Xu, Xiaoming Yu, Junwei Zha, Xiu Li, and Wanhua Li. Reparo: Compositional 3d assets generation with differentiable 3d layout alignment. In *ICCV*, 2025. 3
- [20] Roberto Henschel, Levon Khachatryan, Hayk Poghosyan, Daniil Hayrapetyan, Vahram Tadevosyan, Zhangyang Wang, Shant Navasardyan, and Humphrey Shi. Streamingt2v: Consistent, dynamic, and extendable long video generation from text. In *CVPR*, 2025. 2
- [21] Jonathan Ho, Tim Salimans, Alexey Gritsenko, William Chan, Mohammad Norouzi, and David J Fleet. Video diffusion models. In *NeurIPS*, 2022. 2
- [22] Jiwoo Hong, Noah Lee, and James Thorne. Orpo: Monolithic preference optimization without reference model. In *EMNLP*, 2024. 3
- [23] Edward J Hu, Yelong Shen, Phillip Wallis, Zeyuan Allen-Zhu, Yuanzhi Li, Shean Wang, Lu Wang, and Weizhu Chen. LoRA: Low-rank adaptation of large language models. In *ICLR*, 2022. 6, 7, 19
- [24] Yujia Hu, Songhua Liu, Xingyi Yang, and Xinchao Wang. Flash sculptor: Modular 3d worlds from objects. *arXiv preprint arXiv:2504.06178*, 2025. 3
- [25] Siyuan Huang, Siyuan Qi, Yixin Zhu, Yinxue Xiao, Yuanlu Xu, and Song-Chun Zhu. Holistic 3d scene parsing and reconstruction from a single rgb image. In *ECCV*, 2018. 3
- [26] Xinyu Huang, Yi-Jie Huang, Youcai Zhang, Weiwei Tian, Rui Feng, Yuejie Zhang, Yanchun Xie, Yaqian Li, and Lei Zhang. Open-set image tagging with multi-grained text supervision. In *MM*, 2025. 4
- [27] Zehuan Huang, Yuan-Chen Guo, Xingqiao An, Yunhan Yang, Yangguang Li, Zi-Xin Zou, Ding Liang, Xihui Liu, Yan-Pei Cao, and Lu Sheng. Midi: Multi-instance diffusion for single image to 3d scene generation. In *CVPR*, 2025. 2, 3
- [28] Bernhard Kerbl, Georgios Kopanas, Thomas Leimkühler, George Drettakis, et al. 3d gaussian splatting for real-time radiance field rendering. *TOG*, 42(4):139–1, 2023. 2
- [29] Hyeonwoo Kim, Jeonghwan Kim, Kyungwon Cho, and Hanbyul Joo. Devi: Physics-based dexterous human-object interaction via synthetic video imitation. In *arXiv:2604.20841*, 2026. 9
- [30] Black Forest Labs. FLUX.2: Frontier Visual Intelligence. <https://bfl.ai/blog/flux-2>, 2025. 19
- [31] Qixuan Li, Chao Wang, Zongjin He, and Yan Peng. Phip-g: Physics-guided text-to-3d compositional scene generation. *arXiv preprint arXiv:2502.00708*, 2025. 3
- [32] Ruining Li, Chuanxia Zheng, Christian Rupprecht, and Andrea Vedaldi. Dso: Aligning 3d generators with simulation feedback for physical soundness. In *ICCV*, 2025. 2, 3, 6
- [33] Zhanhao Liang, Yuhui Yuan, Shuyang Gu, Bohan Chen, Tiankai Hang, Mingxi Cheng, Ji Li, and Liang Zheng. Aesthetic post-training diffusion models from generic preferences with step-by-step preference optimization. In *CVPR*, 2025. 3
- [34] Guying Lin, Kemeng Huang, Michael Liu, Ruihan Gao, Hanke Chen, Lyuhao Chen, Beijia Lu, Taku Komura, Yuan Liu, Jun-Yan Zhu, et al. Pat3d: Physics-augmented text-to-3d scene generation. *arXiv preprint arXiv:2511.21978*, 2025. 3
- [35] Lu Ling, Chen-Hsuan Lin, Tsung-Yi Lin, Yifan Ding, Yu Zeng, Yichen Sheng, Yunhao Ge, Ming-Yu Liu, Aniket Bera, and Zhaoshuo Li. Scenethesis: A language and vision agentic framework for 3d scene generation. *arXiv preprint arXiv:2505.02836*, 2025. 3
- [36] Yaron Lipman, Ricky T. Q. Chen, Heli Ben-Hamu, Maximilian Nickel, and Matt Le. Flow matching for generative modeling. In *ICLR*, 2023. 6
- [37] Ilya Loshchilov and Frank Hutter. Decoupled weight decay regularization. *arXiv preprint arXiv:1711.05101*, 2017. 7

- [38] Yu Meng, Mengzhou Xia, and Danqi Chen. Simpo: Simple preference optimization with a reference-free reward. *NeurIPS*, 2024. 3
- [39] Yanxu Meng, Haoning Wu, Ya Zhang, and Weidi Xie. Scenegen: Single-image 3d scene generation in one feedforward pass. In *3DV*, 2026. 2
- [40] Junfeng Ni, Yixin Chen, Bohan Jing, Nan Jiang, Bin Wang, Bo Dai, Puhao Li, Yixin Zhu, Song-Chun Zhu, and Siyuan Huang. Phyrecon: Physically plausible neural scene reconstruction. *NeurIPS*, 2024. 3
- [41] Long Ouyang, Jeffrey Wu, Xu Jiang, Diogo Almeida, Carroll Wainwright, Pamela Mishkin, Chong Zhang, Sandhini Agarwal, Katarina Slama, Alex Ray, et al. Training language models to follow instructions with human feedback. *NeurIPS*, 2022. 3
- [42] Xiaqing Pan, Nicholas Charron, Yongqian Yang, Scott Peters, Thomas Whelan, Chen Kong, Omkar Parkhi, Richard Newcombe, and Yuheng Carl Ren. Aria digital twin: A new benchmark dataset for egocentric 3d machine perception. In *ICCV*, 2023. 7, 8, 14, 21, 22
- [43] Stefan Popov, Pablo Bauszat, and Vittorio Ferrari. Corenet: Coherent 3d scene reconstruction from a single rgb image. In *ECCV*, 2020. 3
- [44] Rafael Rafailov, Archit Sharma, Eric Mitchell, Christopher D Manning, Stefano Ermon, and Chelsea Finn. Direct preference optimization: Your language model is secretly a reward model. In *NeurIPS*, 2023. 3, 6
- [45] Xuanchi Ren, Tianchang Shen, Jiahui Huang, Huan Ling, Yifan Lu, Merlin Nimier-David, Thomas Müller, Alexander Keller, Sanja Fidler, and Jun Gao. Gen3c: 3d-informed world-consistent video generation with precise camera control. In *CVPR*, 2025. 2
- [46] Tobias Sautter, Jan-Niklas Dihlmann, and Hendrik Lensch. 3d-re-gen: 3d reconstruction of indoor scenes with a generative framework. *arXiv preprint arXiv:2512.17459*, 2025. 7, 8, 14, 21
- [47] Oriane Siméoni, Huy V Vo, Maximilian Seitzer, Federico Baldassarre, Maxime Oquab, Cijo Jose, Vasil Khalidov, Marc Szafraniec, Seungeun Yi, Michaël Ramamonjisoa, et al. Dinov3. *arXiv preprint arXiv:2508.10104*, 2025. 15
- [48] Uriel Singer, Adam Polyak, Thomas Hayes, Xi Yin, Jie An, Songyang Zhang, Qiyuan Hu, Harry Yang, Oron Ashual, Oran Gafni, et al. Make-a-video: Text-to-video generation without text-video data. In *ICLR*, 2023. 2
- [49] Ioan A Sucas, Mark Moll, and Lydia E Kavraki. The open motion planning library. *RAM*, 19(4):72–82, 2012. 9, 21
- [50] Gemini Team, Rohan Anil, Sebastian Borgeaud, Jean-Baptiste Alayrac, Jiahui Yu, Radu Soricut, Johan Schalkwyk, Andrew M Dai, Anja Hauth, Katie Millican, et al. Gemini: a family of highly capable multimodal models. *arXiv preprint arXiv:2312.11805*, 2023. 4, 8, 14
- [51] Emanuel Todorov, Tom Erez, and Yuval Tassa. Mujoco: A physics engine for model-based control. In *2012 IEEE/RSJ International Conference on Intelligent Robots and Systems*, 2012. 7, 8
- [52] Bram Wallace, Meihua Dang, Rafael Rafailov, Linqi Zhou, Aaron Lou, Senthil Purushwalkam, Stefano Ermon, Caiming Xiong, Shafiq Joty, and Nikhil Naik. Diffusion model alignment using direct preference optimization. In *CVPR*, 2024. 3, 6
- [53] Ruicheng Wang, Sicheng Xu, Yue Dong, Yu Deng, Jianfeng Xiang, Zelong Lv, Guangzhong Sun, Xin Tong, and Jiaolong Yang. Moge-2: Accurate monocular geometry with metric scale and sharp details. *arXiv preprint arXiv:2507.02546*, 2025. 4
- [54] Bowen Wen, Wei Yang, Jan Kautz, and Stan Birchfield. Foundationpose: Unified 6d pose estimation and tracking of novel objects. In *CVPR*, 2024. 4, 15
- [55] Tong Wu, Guandao Yang, Zhibing Li, Kai Zhang, Ziwei Liu, Leonidas Guibas, Dahua Lin, and Gordon Wetzstein. Gpt-4v(ision) is a human-aligned evaluator for text-to-3d generation. In *CVPR*, 2024. 8, 9
- [56] Chong Xia, Kai Zhu, Zizhuo Wang, Fangfu Liu, Zhizheng Zhang, and Yueqi Duan. Simrecon: Simready compositional scene reconstruction from real videos, 2026. 3
- [57] Pradyumna Yalandur Muralidhar, Yuxuan Xue, Xianghui Xie, Margaret Kostyrko, and Gerard Pons-Moll. Physic: Physically plausible 3d human-scene interaction and contact from a single image. In *ACM SIGGRAPH Asia*, 2025. 3

- [58] Han Yan, Mingrui Zhang, Yang Li, Chao Ma, and Pan Ji. Phycage: Physically plausible compositional 3d asset generation from a single image. *arXiv preprint arXiv:2411.18548*, 2024. 3
- [59] Jianwei Yang, Hao Zhang, Feng Li, Xueyan Zou, Chunyuan Li, and Jianfeng Gao. Set-of-mark prompting unleashes extraordinary visual grounding in gpt-4v. *arXiv preprint arXiv:2310.11441*, 2023. 14
- [60] Kai Yang, Jian Tao, Jiafei Lyu, Chunjiang Ge, Jiabin Chen, Weihang Shen, Xiaolong Zhu, and Xiu Li. Using human feedback to fine-tune diffusion models without any reward model. In *CVPR*, 2024. 3
- [61] Kaixin Yao, Longwen Zhang, Xinhao Yan, Yan Zeng, Qixuan Zhang, Wei Yang, Lan Xu, Jiayuan Gu, and Jingyi Yu. Cast: Component-aligned 3d scene reconstruction from an rgb image. In *SIGGRAPH*, 2025. 2, 3
- [62] Hong-Xing Yu, Haoyi Duan, Charles Herrmann, William T. Freeman, and Jiajun Wu. Wonderworld: Interactive 3d scene generation from a single image. In *CVPR*, 2025. 2
- [63] Wangbo Yu, Jinbo Xing, Li Yuan, Wenbo Hu, Xiaoyu Li, Zhipeng Huang, Xiangjun Gao, Tien-Tsin Wong, Ying Shan, and Yonghong Tian. Viewcrafter: Taming video diffusion models for high-fidelity novel view synthesis. *TPAMI*, 2025. 2
- [64] Jensen Zhou, Hang Gao, Vikram Voleti, Aaryaman Vasishtha, Chun-Han Yao, Mark Boss, Philip Torr, Christian Rupprecht, and Varun Jampani. Stable virtual camera: Generative view synthesis with diffusion models. In *ICCV*, 2025. 2

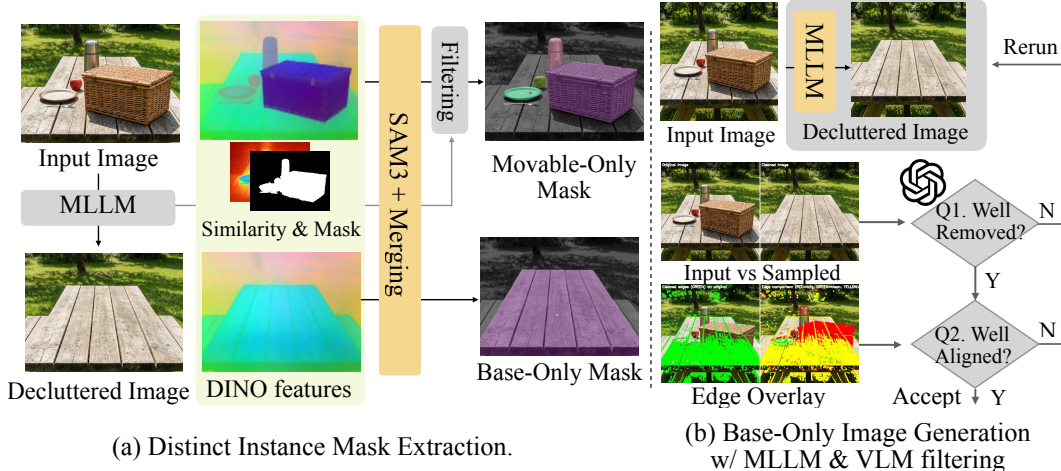


Figure 6: **Distinct Instance Extraction and Declobbered Image I_{base} Generation.** (a) We generate a decluttered image I_{base} via MLLM [50] and compute an object probability map from pixel differences with the original image. Candidate masks in the original image are filtered by their overlap with this map to identify liftable instances, while masks in the decluttered image are selected using Set-of-Mark-based VLM filtering [59] due to the simplified scene layout. (b) We generate a decluttered image by using an MLLM to remove foreground objects. A VLM gate verifies removal completeness and edge alignment with the input, and the generation–verification process is repeated until the acceptance criteria are met.

Method	GraspClutter6D			AriaDigitalTwin					GenWild		
	IoU _{fh/fo} ↑	IoU ↑	Stab. ↑	IoU _{fh/fo} ↑	IoU ↑	3D IoU _{fh/fo} ↑	3D IoU ↑	Stab. ↑	IoU _{fh/fo} ↑	IoU ↑	Stab. ↑
SAM3D [12]	0.055	0.081	0.7%	0.064	0.115	0.045	0.062	0.5%	0.205	0.246	3.2%
Gen3DSR [3] (our bg)	0.007	0.020	0.0%	0.063	0.110	0.183	0.236	0.0%	0.086	0.119	0.4%
Gen3DSR [3]	0.005	0.197	0.0%	0.004	0.551	0.011	0.236	0.0%	0.036	0.461	0.0%
3D-RE-GEN [46] (our bg)	0.019	0.037	3.0%	0.037	0.061	0.059	0.082	0.0%	0.104	0.136	14.8%
3D-RE-GEN [46]	0.015	0.024	0.0%	0.029	0.041	0.061	0.082	0.0%	0.005	0.007	1.3%
Ours	0.213	0.227	34.7%	0.234	0.275	0.286	0.331	31.5%	0.494	0.519	58.4%

Table 4: **Supplementary IoU-based quantitative comparison.** 2D IoU on GraspClutter6D [5] and GenWild; AriaDigitalTwin [42] reports both 2D IoU and ADT 3D IoU. Stab. is the stabilized free-object ratio; columns marked ↑ (↓) indicate higher (lower) is better.

A Implementation Details for the Method

This appendix expands the technical details that were deferred from Sec. 3.

A.1 Preprocessing Pipeline

Declobbered image generation. The base structures mentioned in Sec. 3.1 are selected in a category-wise manner. Thus, depending on the scene, the selected base structure may consist of either a single object instance or multiple object instances. The benefit of using a decluttered image becomes more pronounced in complex scenes, while this step can optionally be omitted for simple scenes with few objects and little to no occlusion.

VLM quality-gate retry loop for base-only image generation. The MLLM-based image editor is invoked up to R_{base} times per scene. On each attempt, a VLM-based quality gate evaluates two criteria on the resulting image: (i) all foreground objects have been removed, and (ii) the base structure remains intact without hallucinated additions. Samples that fail either criterion are re-generated with a fresh sampling seed. The first sample to pass both criteria is accepted as I_{base} ; if all attempts fail, the highest-scoring sample under the VLM gate is retained.

Cross-path de-duplication via DINOv3. The two extraction paths described in Sec. 3.1 can both fire on the same physical structure: SAM3 on I may segment a support structure (e.g., a desk edge) as a placed-object candidate, while SAM3D on I_{base} has already lifted that support structure into the base

structure mesh. DINOv3 [47] resolves this by comparing dense features of I and I_{base} and flagging the region that was actually edited away. Concretely, dense feature maps $\mathbf{F}, \mathbf{F}_{\text{base}} \in \mathbb{R}^{H \times W \times C}$ are extracted, and a per-pixel cosine difference is computed:

$$\Delta(\mathbf{p}) = 1 - \frac{\mathbf{F}(\mathbf{p}) \cdot \mathbf{F}_{\text{base}}(\mathbf{p})}{\|\mathbf{F}(\mathbf{p})\| \|\mathbf{F}_{\text{base}}(\mathbf{p})\|}. \quad (12)$$

Thresholding Δ at δ_{dino} produces a binary edited-region map $P = \mathcal{K}[\Delta > \delta_{\text{dino}}]$ that marks the pixels in I that no longer appear in I_{base} . A placed-object-path candidate mask M_j is retained only if its footprint sufficiently overlaps P :

$$|M_j \cap P| / |M_j| > \alpha_{\text{mask}}, \quad (13)$$

otherwise the mask falls outside the edited region and is dropped to avoid duplicating a support structure that the base path has already lifted. Fig. 6 summarizes this pipeline.

Floor and wall plane extraction with Manhattan rectification. Plane extraction runs in two passes. The first pass operates on raw monocular depth and SAM3 segmentation, before any object fitting. SAM3 masks for floor and ground regions are back-projected to 3D via metric depth and fitted with RANSAC (5 cm residual, with the constraint that the floor normal points downward in OpenCV convention). Wall masks (queried on original image I) are fitted per-wall (1 cm RANSAC residual); orientation clusters are formed via DBSCAN, mutual orthogonality is verified, and the top four walls by coverage are retained. Manhattan rectification then selects the up direction by a priority order: cross-product of two orthogonal walls, otherwise the floor-derived up, otherwise a mesh-derived fallback; all wall normals are rectified perpendicular to the chosen up.

Post-fit plane re-extraction and tabletop refinement. After the per-object fitter runs, the plane stack is re-extracted using the fitted meshes, since they provide a stronger up-direction signal than depth alone. The floor offset is snapped to the lowest vertex of the union of fitted meshes, which removes the residual gap between sit-on-floor objects and the floor plane. For objects whose VLM phrase indicates a table or desk, an additional 4-DOF refinement is applied to the table mesh: yaw, in-plane translation (x, y) , and isotropic log-scale are optimized jointly via Adam against the Chamfer distance to the depth-derived top-surface point cloud, with regularization toward the initial pose to resist mode-switching on symmetric tables. The top vertex of the refined table mesh is then snapped to the detected table plane, so that objects placed on top rest flush against it during simulation.

A.2 Pose Alignment Details

Translation–Scale Initial Alignment. Before applying FoundationPose [54] in Eq. 3, we perform a lightweight translation–scale alignment for each SAM3D object. Although FoundationPose is effective as a local pose refiner, we find that it is sensitive to large errors in the initial scale or object center: when the rendered object is substantially misaligned with the observed mask and depth, the render-and-compare refinement can converge to an incorrect pose or fail to recover. We therefore use the masked depth observation to bring the SAM3D prediction into a reasonable basin before FoundationPose. Given the canonical mesh $\mathcal{M}_i^{\text{init}}$, initial prediction $(\mathbf{R}_i^{\text{init}}, \mathbf{t}_i^{\text{init}}, s_i^{\text{init}})$, and the target point cloud \mathcal{P}_i back-projected from the masked depth map, we solve only for the isotropic scale and translation (s_i, \mathbf{t}_i) while keeping $\mathbf{R}_i^{\text{init}}$ fixed. We avoid optimizing rotation in this stage because chamfer-style point-set losses provide weak and often degenerate rotation signals under monocular occlusion, partial visibility, and symmetric or textureless geometry. Thus, this step is intended not as a full pose solver, but as a robust 4-DoF initialization that corrects scale and centering errors before the subsequent rotation-aware refinement.

Since SAM3D meshes are complete while the input depth observes only the visible surface, directly matching all mesh vertices to \mathcal{P}_i biases the alignment toward self-occluded geometry. We therefore rasterize $\mathcal{M}_i^{\text{init}}$ once at the initial pose and keep only the visible vertex subset $\mathcal{V}_i^{\text{vis}}$. The translation–scale alignment is then optimized with a one-sided chamfer objective from the observed point cloud to the visible mesh vertices:

$$\mathcal{L}_{\text{align}}(s_i, \mathbf{t}_i) = \frac{1}{|\mathcal{P}_i|} \sum_{\mathbf{y} \in \mathcal{P}_i} \min_{\mathbf{v} \in \mathcal{V}_i^{\text{vis}}} \|\mathbf{y} - (s_i \mathbf{R}_i^{\text{init}} \mathbf{v} + \mathbf{t}_i)\|_2. \quad (14)$$

The asymmetric direction encourages the predicted visible surface to cover the observed depth points, while avoiding penalties from unobserved mesh regions caused by self-occlusion or inter-object occlusion.

However, the one-sided loss alone can favor over-grown meshes, since a large mesh may still cover all observed points. To reduce this failure mode, we run multi-start Adam optimization from several initial scales $s_{i,0}^{(k)} = \rho_k s_i^{\text{init}}$, with $\rho_k \in \{0.5, 0.75, 1.0, 1.25\}$, and apply a weak log-scale prior:

$$\mathcal{L}^{(k)} = \mathcal{L}_{\text{align}}(s_i, \mathbf{t}_i) + \lambda (\log s_i - \log s_i^{\text{init}})^2. \quad (15)$$

After convergence, we rank the candidates using a combination of silhouette recall and a weakly weighted bidirectional chamfer score:

$$k^* = \arg \max_k \frac{1}{2} \widetilde{\text{Recall}}^{(k)} + \frac{1}{2} (1 - \widetilde{\mathcal{L}}_{\text{bi}}^{(k)}), \quad (16)$$

where the recall term penalizes under-coverage of the input mask, and the bidirectional chamfer term discourages excessive scale growth. The selected (s_i^*, \mathbf{t}_i^*) is then used as the initialization for FoundationPose, while the rotation remains initialized by $\mathbf{R}_i^{\text{init}}$.

Tabletop-Plane Refinement. For tables and desks, even small residual tilt or height errors on the top support surface produce visible floating or penetration artifacts once small objects are placed on top. We therefore add a category-gated refinement stage after FoundationPose that aligns the mesh top surface to an upper plane detected from MoGe depth.

Given the post-refinement mesh and the scene up direction \mathbf{u} , we first extract a depth-supported tabletop plane $(\mathbf{n}^d, \mathbf{p}^d)$ by filtering upward-facing pixels within the object mask, applying a height-band constraint to suppress clutter and under-shelf regions, and fitting a plane with RANSAC. We also estimate the mesh top plane $(\mathbf{n}^m, \mathbf{p}^m)$ from canonical top vertices identified along the transformed up direction. The mesh top is then rigidly snapped onto the detected support plane by aligning normals and removing the residual height gap:

$$T_{\text{snap}}(v) = \mathbf{R}^{\text{snap}} v + (\mathbf{p}^m - \mathbf{R}^{\text{snap}} \mathbf{p}^m) + \delta, \quad (17)$$

where \mathbf{R}^{snap} rotates \mathbf{n}^m onto \mathbf{n}^d , and $\delta = ((\mathbf{p}^d - \mathbf{p}^m) \cdot \mathbf{n}^d) \mathbf{n}^d$ translates the mesh along the detected plane normal to close the residual gap to the support plane.

Starting from the snapped pose, we further optimize four residual degrees of freedom consisting of yaw rotation around the detected plane normal, two in-plane translations, and an isotropic scale. The optimization minimizes a symmetric chamfer between the rendered visible mesh point cloud and the depth-lifted observation, regularized toward the snapped initialization:

$$\min_{\theta, t_x, t_y, \log s} \frac{1}{2} (d_{\hat{P} \rightarrow P} + d_{P \rightarrow \hat{P}}) + \lambda [(\theta/\theta_0)^2 + (t_x/t_0)^2 + (t_y/t_0)^2 + (\log s/\sigma_0)^2]. \quad (18)$$

This refinement is only applied to objects whose semantic label matches `table` or `desk`; otherwise the FoundationPose result is kept unchanged. We additionally reject unstable refinements using a set of geometric sanity checks, including insufficient plane support, non-horizontal detected planes, and floor-plane degeneracies.

A.3 Gravity-Based Diagnostics Details

How VLM tags object-specific pose DoF. Indoor scenes routinely contain objects that are not floor-supported — picture frames, wall-mounted TVs, pendant lamps — which the physics simulator would otherwise drop to the ground and corrupt the reconstructed layout. To handle these, we run a per-object vision-language query on the input image: for each detected mesh, we composite a two-panel image that highlights the target with a colored mask, bounding box, and label on the left and isolates it against a desaturated background on the right, then ask the VLM to classify the object as standing or hanging under a strict own-attachment-only rule (an object resting on a wall-mounted shelf remains standing; only the shelf itself is hanging). For hanging objects we additionally elicit a pin count — one for freely swinging mounts (hooks, pendants) and two for rigid mounts (frames, brackets) — which the simulator uses to anchor the object with the appropriate number of constraints. The full prompt and qualitative examples are provided in Fig. 7.

Wall-anchoring Mechanism For each object o flagged as *hanging* by the VLM with pin count $K \in \{1, 2\}$, we attach it to the reconstructed scene wall through K ball-joint anchors. Each anchor is

Pose-DoF Extraction Prompt

[ROLE]
You are an expert at analyzing how objects are physically supported in indoor scenes.

[TASK]
Determine whether a specific highlighted object is "standing" (resting on a surface via gravity) or "hanging" (directly attached to a wall/ceiling, and would fall if that attachment were removed).

[CRITICAL RULE]
Only classify the object's OWN attachment. Do NOT trace the support chain further. If an object is simply resting on top of something — even a wall-mounted shelf — it is "standing". Whether the shelf itself is hanging is irrelevant.

[INSTRUCTION]
Analyze the highlighted object in the image.

[IMAGE LAYOUT]
- LEFT : Scene with the target object highlighted (colored mask overlay + bounding box + label)
- RIGHT : Same scene with background desaturated to grayscale — the full-color region is the target object

[TARGET OBJECT]
- Mesh index : {idx}
- Description : "phrase"
- Bounding box : [{x1}, {y1}, {x2}, {y2}]

[REASONING PROTOCOL]
Determine this object's physical support type. You MUST reason through these steps explicitly:

[STEP 1 — IDENTIFY THE OBJECT]
What is this object and where exactly is it in the scene?

[STEP 2 — HOW IS THIS OBJECT ITSELF SUPPORTED?]
Ask: "If only remove this object's own attachment point, does it fall?"
- Is it RESTING ON a surface (floor, desk, shelf, another object)? Gravity keeps it there with no attachment needed → "standing".
- Is it DIRECTLY ATTACHED to a wall or ceiling (screwed, bolted, nailed, hung on a hook)? Removing that attachment causes it to fall → "hanging".
- STOP HERE. Do NOT ask whether the surface it rests on is itself hanging or floor-connected. That is irrelevant.

[STEP 2 — EXAMPLES]
- Book on a wall-mounted shelf
→ book just RESTS on shelf surface
→ "standing" (the shelf's status is irrelevant)
- Vase on a floating desk
→ vase RESTS on desk → "standing"
- Wall-mounted shelf itself
→ shelf is ATTACHED to wall, remove attachment → falls
→ "hanging"
- Picture frame hung on a nail
→ frame is ATTACHED to wall → "hanging"
- Coat on a hook
→ coat is ATTACHED to hook → "hanging"
- TV on a TV stand
→ TV RESTS on stand → "standing"
- Wall-mounted TV
→ TV is ATTACHED to wall bracket → "hanging"
- Object leaning against wall but sitting on floor
→ RESTS on floor → "standing"

[STEP 3 — PIN COUNT] (Only if hanging)
- 1 pin : hangs from a single point, could swing/rotate (e.g., coat on hook, hanging plant, pendant lamp)
- 2 pins : rigidly mounted at multiple points, cannot rotate (e.g., picture frame, wall-mounted TV, mirror, towel rack, shelf brackets)

[OUTPUT FORMAT]
Return ONLY valid JSON (no markdown, no extra text):
{
 "step1_identify" : "what is this object and where is it?",
 "step2_own_support" : "how is THIS object supported? resting on what surface, OR attached to what wall/ceiling point?",
 "support" : "standing" or "hanging",
 "standing_on" : "the immediate surface/object it rests on (e.g., 'wall-mounted shelf', 'floor', 'wooden desk'). Use null if hanging.",
 "hanging_from" : "what it is directly mounted/hung on (e.g., 'wall nail', 'ceiling bracket', 'wall hook'). Use null if standing.",
 "num_pins" : 0 for standing, 1 or 2 for hanging
}

Example Outputs



A:
- support: hanging
- num_pins: 2
- hanging_from: wall
- standing_on : None

➔ *line-anchored* (1-DoF)



A:
- support: standing
- num_pins: 0
- hanging_from: None
- standing_on : wall-mounted shelf

➔ *free* (6-DoF)

Figure 7: **VLM-based wall-hang detection.** Each object is rendered into a two-panel query image — highlighted overlay (left) and color-on-grayscale isolation (right) — and classified by a VLM as standing or hanging under an own-attachment-only rule, with hanging objects additionally tagged with a pin count (0: free, 1: point-anchored, 2: line-anchored).

a pair: a point $\mathbf{p}_o^{(k)}$ on the object's surface and its mate $\mathbf{p}_W^{(k)}$ on the wall surface, which the simulator forces to coincide in world space throughout the rollout. The procedure has three parts.

(1) Choosing the object-side pin. We restrict pin candidates to vertices that are simultaneously near the top of the object (along the anti-gravity direction) and on its wall-facing back side, excluding front- or bottom-facing vertices that would otherwise yield an inverted or wall-detached hang. From this top-back region we then select pins by case: for $K = 1$ (hooks, pendant lamps, and other freely swinging mounts) we take the highest and most laterally centered vertex so the object hangs evenly; for $K = 2$ (picture frames, mounted TVs, and other rigid mounts) we take the leftmost and rightmost vertices along the wall-parallel horizontal direction — i.e. the top-left and top-right corners of the wall-facing back — so that the two anchors together keep the mounted face flat against the wall.

(2) Pairing each pin with a wall point. Each object-side pin is paired with its closest point on the wall mesh — the foot of the perpendicular dropped from the pin onto the wall surface. This preserves the natural standoff distance between the object and the wall (frame thickness, hook offset, etc.) rather than collapsing the object onto the wall plane.

(3) Force coupling between the two points. Each pin pair is realized as a MuJoCo ball-joint equality constraint that ties the object-side and wall-side points together so they coincide in world space at every simulation step, regardless of how the object moves. Whenever the object tries to fall, slide, or rotate away from an anchor, the solver applies an equal-and-opposite reaction force on the object and on the (static) wall along the violation direction, acting as a stiff but critically damped spring-damper rather than a hard weld so that contact transients are absorbed without instability.

Physics-mode parameters. The simulator runs at a fine timestep $\Delta t_{\text{sim}} = 1/480$ s, which is required because the contact stiffness time constant must satisfy $\geq 2\Delta t_{\text{sim}}$ for the implicit integrator to remain stable. Contacts are configured to be inelastic and stiff (damping ratio 2.0, time constant 0.01 s); friction coefficients (sliding, torsional, rolling) are set to (1.0, 0.95, 0.01) with contact dimensionality four.

Penetration Resolution. For each newly placed object we run a per-object overlap-resolution pass against the floor, the rectified walls and every previously placed object: the new object is the sole

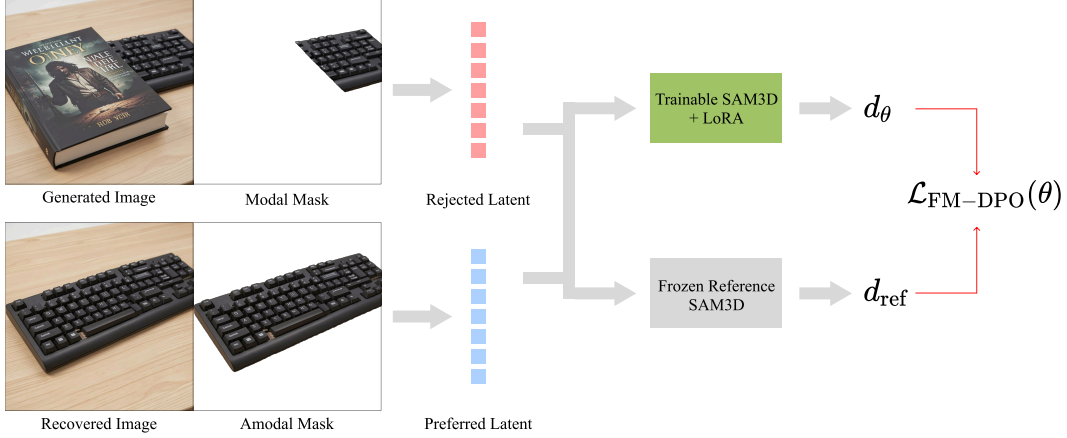


Figure 8: **SAM3D Fine-tuning Pipeline** We fine-tune SAM3D for amodal shape resampling using synthetic preference pairs that contrast occlusion-failed latents with completed amodal latents. A flow-matching DPO objective updates only LoRA adapters while keeping the reference SAM3D frozen, and the resulting model is used at test time for physics-informed resampling.

dynamic body. At every iteration we read the resulting contact list from MuJoCo, partition the contacts into priority groups (environment \succ static), and select the highest-priority non-empty group so that floor and wall penetrations are always resolved before contacts with previously placed objects. We then translate the dynamic object by $(d_i^{\max} + 7 \text{ mm})$ along the depth-weighted average normal $\hat{\mathbf{n}}_i = \text{normalize}(\sum_k d_{i,k} \mathbf{n}_{i,k})$ of the selected group. The loop terminates when the contact list empties or after 200 iterations. If the cumulative displacement exceeds 0.3 m or any contact survives, the object is flagged as physics-disabled and excluded from the diagnostic simulation rather than allowed to corrupt the rest of the scene.

A.4 Shape Correction Details

Gravity-axis Stretch Details. For objects corrected by gravity-axis stretching, we use the signed displacement η_i from Eq. (9). We orient the gravity-aligned OBB axis such that $(\hat{\mathbf{u}}_i^{\text{grv}})^\top \mathbf{g} \geq 0$, and define its canonical-frame counterpart as

$$\hat{\mathbf{a}}_i^{\text{grv}} = (\mathbf{R}_i^{\text{pre}})^\top \hat{\mathbf{u}}_i^{\text{grv}}. \quad (19)$$

The stretch factor is

$$\lambda_i = 1 + \eta_i. \quad (20)$$

We first apply anisotropic stretching in the canonical mesh frame:

$$\bar{\mathcal{M}}_i^{\text{str}} = \text{Stretch}_{\hat{\mathbf{a}}_i^{\text{grv}}}(\mathcal{M}_i^{\text{init}}; \lambda_i), \quad (21)$$

where $\text{Stretch}_{\hat{\mathbf{a}}}(\mathcal{M}; \lambda)$ anisotropically scales the mesh by factor λ along axis $\hat{\mathbf{a}}$ while leaving the orthogonal directions unchanged. For a vertex \mathbf{v} of a canonical mesh centered at the origin, this operation is

$$\mathbf{v}' = \lambda_i (\mathbf{v}^\top \hat{\mathbf{a}}_i^{\text{grv}}) \hat{\mathbf{a}}_i^{\text{grv}} + (\mathbf{I} - \hat{\mathbf{a}}_i^{\text{grv}} (\hat{\mathbf{a}}_i^{\text{grv}})^\top) \mathbf{v}. \quad (22)$$

Let γ_i be the longest side length of the AABB of $\bar{\mathcal{M}}_i^{\text{str}}$. To preserve the canonical-mesh convention, we renormalize the stretched mesh and absorb the normalization factor into the object scale:

$$\mathcal{M}_i^{\text{str}} = \frac{1}{\gamma_i} \bar{\mathcal{M}}_i^{\text{str}}, \quad s_i^{\text{str}} = \gamma_i s_i^*. \quad (23)$$

Finally, we update the translation so that the OBB face opposite to gravity remains fixed:

$$\mathbf{t}_i^{\text{str}} = \mathbf{t}_i^{\text{pre}} + \frac{1}{2} \eta_i \ell_i^{\text{pre}} \hat{\mathbf{u}}_i^{\text{grv}}. \quad (24)$$

Thus, stretching changes the object geometry, scale, and translation, while preserving the corrected rotation from diagnostic simulation.

SAM3D Fine-tuning Details. We construct two types of preference pairs for fine-tuning SAM3D under the resampling input in Eq. (10). First, for occlusion-completion pairs, we synthesize paired-object scenes using a text-to-image generator [30], where one object substantially occludes the target object. An image-to-image editor [30] then removes the occluding object and completes the full shape of the target object. From the original occluded image, we extract the modal mask M_i , while from the edited image, we extract a full-object mask M'_i that serves as an amodal crop mask. We run SAM3D on both images to obtain shape latents: the latent from the occluded input is treated as the rejected sample x_i^- , and the latent from the edited full-object input is treated as the preferred sample x_i^+ . During fine-tuning, the condition $c_i = (I, M_i, I_{M'_i}, D)$ follows the same input setting as Eq. (10).

We additionally construct clean preservation pairs to avoid degrading SAM3D’s original input behavior. For these pairs, we synthesize scenes containing an unoccluded object, obtain its segmentation mask, and run SAM3D to produce a clean latent as x_i^+ . We then corrupt the mask by dropping part of the segmentation and run SAM3D again, using the resulting latent as x_i^- . Thus, occlusion-completion pairs teach amodal completion under the new crop setting, while clean preservation pairs regularize the model to retain its original modal-mask reconstruction ability.

We fine-tune SAM3D using the FM-DPO objective in Eq. (11). Let $\ell_\theta^{\text{shape}}(x, c, t, \epsilon)$ denote the shape-branch flow-matching loss of SAM3D for latent x under condition c , timestep t , and noise ϵ . For each preference pair, we compute the win-lose loss difference of the current model as

$$d_{\theta,i} = \ell_\theta^{\text{shape}}(x_i^+, c_i, t_i, \epsilon_i^+) - \ell_\theta^{\text{shape}}(x_i^-, c_i, t_i, \epsilon_i^-), \quad (25)$$

and the corresponding difference of the frozen reference model as

$$d_{\text{ref},i} = \ell_{\theta_{\text{ref}}}^{\text{shape}}(x_i^+, c_i, t_i, \epsilon_i^+) - \ell_{\theta_{\text{ref}}}^{\text{shape}}(x_i^-, c_i, t_i, \epsilon_i^-), \quad (26)$$

where θ_{ref} is the frozen base SAM3D model. The current model and the reference model are evaluated on the same condition, timestep, and noise for each preference pair. Therefore, the objective optimizes the preference improvement of the current model relative to the frozen reference, rather than directly minimizing the preferred-sample loss alone.

The sample weight w_i is defined by the pair type:

$$w_i = \begin{cases} 1.0, & \text{if } i \text{ is an occlusion-completion pair,} \\ 0.1, & \text{if } i \text{ is a clean preservation pair.} \end{cases} \quad (27)$$

We assign a larger weight to occlusion-completion pairs because they directly target the amodal resampling failure mode, while clean preservation pairs act as a weaker regularizer.

We do not fine-tune the full SAM3D generator. Instead, we attach LoRA [23] adapters only to the attention projections of the shape generation branch and update these adapters during training. This limits adaptation to the shape latent pathway while preserving the base model’s original reconstruction behavior.

A.5 Sequential Composition Details

Ordering strategy. Dynamic objects are sorted ascending by the projection of their world-frame bounding-box bottom corner onto the gravity axis, so the lowest object is placed first. An alternative ordering based on the lowest point of the depth-lifted input mask was explored but was found unreliable on partially occluded objects whose mask boundary leaks onto neighbouring surfaces; the bounding-box bottom is consistent with the quantity used internally by the penetration resolver and is therefore preferred.

Wall-attached object handling. A VLM [1] classifies each object as either floor-supported or wall-attached (see Sec. A.3). For wall-attached objects, the object is held to the wall by the K ball-joint anchors of Sec. A.3, and any penetration-resolution push is applied subject to these anchor constraints so the object cannot drift away from the wall. Accordingly, a single-pin ($K=1$) object retains 3-DoF rotation about its anchor point, while a two-pin ($K=2$) object retains only 1-DoF rotation about the line joining its two anchors. Without these anchors, wall-supported objects released as fully dynamic bodies tend to rotate or fall away from the wall under penetration-resolution forces, since their visible silhouette underdetermines the wall-normal contact geometry.

Final-pass full settling. Once sequential penetration resolution has placed every object into a collision-consistent assembled scene, we run a single final settling simulation over the whole scene. Unlike the diagnostic probe — which keeps only one object dynamic and freezes it at first contact — here all *free* objects are simultaneously dynamic, simulated as full 6-DoF rigid bodies and allowed to settle jointly under gravity for a fixed duration T_{settle} , while *point-anchored* and *line-anchored* objects stay pinned at their anchors and move only by rotation about the anchor point (3-DoF) or anchor line (1-DoF), respectively. This produces a globally consistent layout in which every object rests in stable equilibrium and is directly usable in a downstream physics simulator. Any object whose displacement during this final pass exceeds the divergence bound $\delta_{\text{max}}^{\text{final}}$ is reverted to its pre-settle pose, which guards against late solver divergence on rare edge cases.

B Experimental Details

This section provides details of the quantitative, qualitative, and application experiments.

B.1 Metrics

Physical plausibility metrics. We evaluate reconstruction quality at *post-sim*, the configuration obtained after a 5 s MuJoCo gravity-settle simulation and report both mask-side and shape-side metrics on each. For mask-side metrics, we render all meshes jointly and compare their corresponding visible rendered mask against input segmentation. We then report (i) **2D IoU**, the mean of identity-paired per-object IoUs between each ground-truth mask and the prediction at the same object index, and (ii) **2D ABO**,

$$\text{ABO}_{2\text{D}} = \frac{1}{N_{\text{gt}}} \sum_{i=1}^{N_{\text{gt}}} \max_{j=1, \dots, M_{\text{pred}}} \text{IoU}(g_i, p_j),$$

with the denominator fixed at the ground-truth count so that missing or filtered-out predictions are penalized as misses rather than hidden. Shape-side metrics are computed against the ADT object library: each ground-truth mesh is placed in the scene frame via its provided pose, transported into the input camera’s frame, and surface-sampled to 10k points.

We report **3D IoU** as the mean axis-aligned-bounding-box (AABB) IoU over matched (GT, pred) pairs and **3D ABO**,

$$\text{ABO}_{3\text{D}} = \frac{1}{N_{\text{gt}}} \sum_{i=1}^{N_{\text{gt}}} \max_j \text{IoU}_{3\text{D}}(B_{g_i}, B_{p_j}),$$

again with denominator N_{gt} ; the AABBs are well-defined because the input-camera-as-identity convention places all predictions in a world-aligned frame.

Free/hanging variants (fh/fo). We compute each metric under two strict settings — fh counts only valid *free* and *hanging* objects, and fo counts only valid *free* objects — and report their average, e.g. $\text{ABO}_{\text{fh/fo}} = \frac{1}{2}(\text{ABO}_{\text{fh}} + \text{ABO}_{\text{fo}})$ (likewise for IoU).

Penetration criterion and Stability. From the post-sim contact set, we flag an object as **penetrating** if and only if at least one of its MuJoCo contact pairs has penetration depth exceeding $\varepsilon = 2$ mm; a single deep contact suffices, and ground versus inter-object penetrations are tracked separately for diagnostics. We report *Stab.* as the fraction of free objects that remain stable after the evaluation simulation. An object is considered stable if its final displacement from the initial pose is below the primary stability threshold, which we set to 5 cm. Objects categorized as hanging or initially penetrating are excluded from the denominator, so this metric measures stability only over freely movable objects.

$$\text{Stab.} = \frac{|\{o \in \mathcal{O}_{\text{free}} : \Delta(o) < 0.05 \text{ m}\}|}{|\mathcal{O}_{\text{free}}|} \times 100.$$

B.2 Mesh Quality Evaluation Details

For each resampling triggered instance, we render every method’s mesh from the original input camera on a white background and concatenate it with the input RGB (with the visible-mask overlay)

into a horizontal triptych: *input / Case A (blue border) / Case B (red border)*. A single VLM judge is queried once per ordered pair with a fixed system + user prompt that asks a single forced-choice question: “which candidate is the more plausible full-object completion of the partially observed occluded instance,”. To remove left/right position bias every unordered pair is queried in both orders.

Given the resulting win counts A_{ij} (number of times method i was preferred over j ; ties contribute +1 to both A_{ij} and A_{ji}), we fit Elo ratings r_i , initialized to 1000, by minimizing the Bradley–Terry negative log-likelihood with the standard Elo scale $c = 400$:

$$\mathcal{L}(r) = \sum_{i \neq j} A_{ij} \log(1 + 10^{(r_j - r_i)/c}), \quad P(i \succ j) = \frac{1}{1 + 10^{(r_j - r_i)/c}}, \quad (28)$$

optimised with Adam (lr = 10^{-1} , 10,000 iterations, float64).

B.3 Aria Digital Twin Preprocessing Details

We build a scenario-balanced evaluation set of 40 frames drawn from 24 Aria Digital Twin (ADT) [42] sequences, selected with five sequences each from the *clean*, *decoration*, *meal*, and *work* scenarios and four from *recognition*. We deliberately exclude the *multiuser* variants (third-party hands appear in frame) and the **_skeleton* releases (mocap-skeleton pixels contaminate the ground-truth segmentation). Within each retained sequence, we automatically pick two frames maximally separated in time, subject to the conjunction of five filters:

- (i) The frame must lie inside the sequence’s GT availability window so that GT depth, segmentation, and 3D bounding boxes are all valid
- (ii) The Aria head-mounted camera must be near-stationary, with linear and angular velocities below 0.6 m/s and 0.6 rad/s respectively
- (iii) Every object marked `motion_type=dynamic` in `instances.json` must have remained spatially static—i.e. its 3D position must vary by less than 10 mm over a ± 5 s rolling window—so that hands have left and the GT 3D state is consistent with the captured RGB
- (iv) The GT segmentation must contain at least ten non-structural object instances, and at least 60% of their pixels must fall inside the central 60% \times 60% image region, ensuring the camera is genuinely looking at the cluttered scene rather than at a wall
- (v) MediaPipe [18] HandLandmarker, applied to both the native and the 90°-rotated frame, must detect zero hands. Each accepted frame is then undistorted from the Aria fisheye model to a pinhole camera, cropped to the largest square inscribed in the valid undistorted region (removing fisheye corner artifacts), and rotated 90° clockwise so that gravity points downward.

Ground-truth per-object masks are derived from the ADT instance segmentation by keeping every instance whose name does not start with the architectural-shell prefixes `Apartment_`, `ApartmentEnv`, or `ApartmentDynamic` (i.e. floors, walls, doors, ceilings) and that additionally has a GT 3D bounding box, a ≥ 100 -pixel footprint, and covers $\geq 0.1\%$ of the image. Built-in furniture and large appliances (refrigerators, kitchen islands, beds) are intentionally retained as physical objects rather than being filtered as architecture, yielding on average ≈ 26 masked objects per scene that are subsequently fed into SAM3D for stage-2 input mesh generation.

B.4 Application Details

Robot-arm Manipulation. We adopt the closed-loop VLM agent of VLMPose [6] as our text-guided 6D goal-pose predictor, using GPT-5.2 with the authors’ default inference-time configuration (4 multi-view cameras, object-centered coordinate visualization, single-axis rotation prediction, and up to 5 evaluator–proposer iterations). The predicted goal pose is passed to GraspNet [16] for grasp proposals on the target object’s mesh-sampled point cloud, and for motion planning OMPL [49] is used for a rectangular lift–translate–lower trajectory on a Franka arm to reduce inter-object collisions.

C Additional Experimental Results

C.1 Additional Quantitative Comparisons

We benchmark Ours against SAM3D [12], Gen3DSR [3], and 3D-RE-GEN [46] on GraspClutter6D [5], Aria Digital Twin (ADT) [42], and GenWild, reporting 2D IoU (fh/fo and identity-paired)

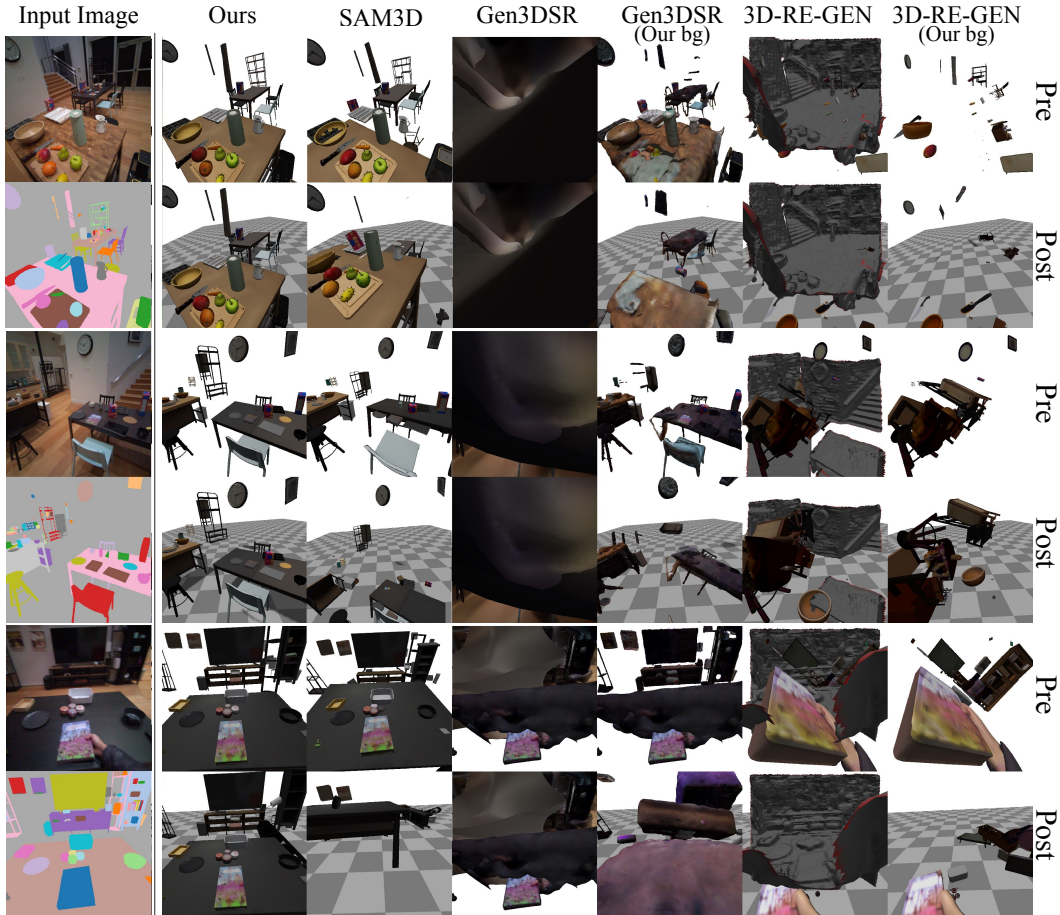


Figure 9: **Qualitative Comparison of ADT.** Additional qualitative comparisons on the ADT dataset.

and Stab., plus 3D IoU on ADT. For Gen3DSR and 3D-RE-GEN we also evaluate a variant that swaps in our background reconstruction (“our bg”) to isolate the foreground predictor from the layout.

Tab. 4 shows that Ours sets the new state of the art across all three datasets, leading on identity-paired IoU, ADT 3D IoU, and most pronouncedly on Stab. This margin reflects the role of gravity-based diagnostics and shape correction in producing layouts that physically settle, rather than merely projecting plausibly into the input view.

C.2 Additional Qualitative Comparisons

We supplement the qualitative comparisons in the main paper with further results on the Aria Digital Twin (ADT) [42] and GraspClutter6D [5] datasets. Fig. 9 extends the ADT comparisons, while Fig. 10 extends those on GraspClutter6D.

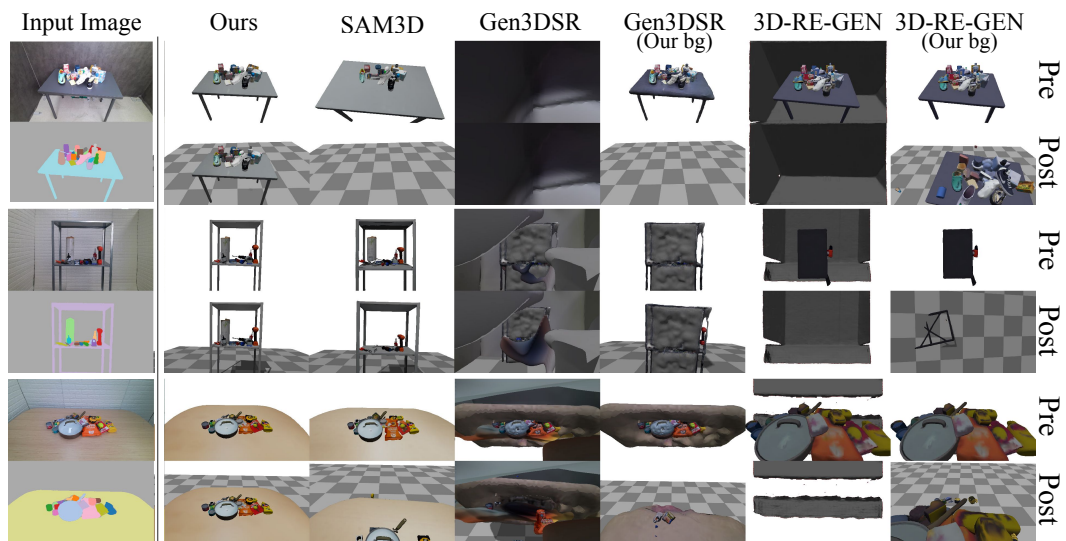


Figure 10: **Qualitative Comparison of GraspClutter6D.** Additional qualitative comparisons on the GraspClutter6D dataset.